Development of a ReaxFF potential for Au–Pd

Yu V Rusalev

The Smart Materials Research Institute, Southern Federal University, 178/24 Sladkova st., 344090 Rostov-on-Don, Russia

E-mail: rusalev@sfedu.ru

A V Motseyko

Institute of Physics, Southern Federal University, 194 Stachki pr., 344090 Rostov-on-Don, Russia

E-mail: moceyko@sfedu.ru

A A Guda

The Smart Materials Research Institute, Southern Federal University, 178/24 Sladkova st., 344090 Rostov-on-Don, Russia

E-mail: guda@sfedu.ru

S A Guda

The Smart Materials Research Institute, Southern Federal University, 178/24 Sladkova st., 344090 Rostov-on-Don, Russia
Institute of mathematics, mechanics and computer science, Southern Federal University, 8a Milchakova st., 344090 Rostov-on-Don, Russia

E-mail: gudasergey@sfedu.ru

A V Soldatov

The Smart Materials Research Institute, Southern Federal University, 178/24 Sladkova st., 344090 Rostov-on-Don, Russia

E-mail: soldatov@sfedu.ru

N V Ter-Oganessian

Institute of Physics, Southern Federal University, 194 Stachki pr., 344090 Rostov-on-Don, Russia

E-mail: teroganesyan@sfedu.ru

Abstract. The bimetallic alloys often outperform their single-component counterparts due to synergistic effects. Being widely known, the Au–Pd alloy is a promising candidate for the novel heterogeneous nanocatalysts. Rational design of such systems requires theoretical simulations under ambient conditions. *Ab initio* quantum-mechanical calculations employ the density functional theory (DFT) and are limited to

the systems with few tens of atoms and short timescales. The alternative solution implies development of reliable atomistic potentials. Among different approaches ReaxFF combines chemical accuracy and low computational costs. However, the development of a new potential is a problem without unique solution and thus requires accurate validation criteria. In this work we construct ReaxFF potential for the Au–Pd system based on *ab initio* DFT calculations for bulk structures, slabs and nanoparticles with different stoichiometry. The validation was performed with molecular dynamics and Monte-Carlo calculations. We present several optimal parametrizations that describe experimental bulk mechanical and thermal properties, atomic order-disorder phase transition temperatures and the resulting ordered crystal structures.

Keywords: Au–Pd alloy, ReaxFF, molecular dynamics, Monte-Carlo method, nanoparticles

1. Introduction

Accelerating chemical reactions is crucial for sustainable economic development and production of pharmaceuticals, fuels, consumer chemicals, etc. In this respect heterogeneous catalysis is of primary importance, since it allows for facile separation of the product and the catalyst. In most industrial applications, e.g., CO_2 reduction, water splitting, or methane activation, metals or metal oxides are used as catalysts. Thus, much effort is focused on research of catalytic properties of various metal alloys, e.g., Ni–Co for methane reforming [1], Heusler alloys for selective hydrogenation of alkynes [2], Pt–Co for water splitting [3], Ir–Cu for oxygen evolution reaction [4], Ag–Au for oxidation and reduction catalysis [5, 6], and Pd–Sb for ethanol oxidation [7].

Pd-based catalysts acquire special attention due to their impressive performance in many reactions [8]. It turns out, that bimetallic Pd-based catalysts (Pd–M) allow optimization and tunability of the number, activity, and selectivity of active sites – the determining factors of the catalytic reaction performance. Among different bimetallic Pd–M variants, the gold-palladium alloys take their prominent role [9]. For example, colloidal solution based on gold-palladium nanoparticles is a promising catalyst for selective methane to methanol oxidation at mild temperatures [10]. Decoration of Au nanoparticles by Pd atoms providing bimetallic Pd–Au surface results in improved CO_2 electroreduction [11], whereas the performance of $Au_{75}Pd_{25}$ nanoparticles for cyclohexane oxidation was found to strongly depend on their form, being higher for icosahedral nanoparticles, than for octahedral ones [12].

Computational approaches have become very helpful for targeted design of catalysts as they may provide atomic-level details of catalytic processes and assist in development of new catalysts with improved performance [13]. Many techniques have been developed that treat the system at different length and time scales. Despite tremendous progress in available computational power and achieved accuracy of various methods like density functional theory (DFT) for solving the Schrödinger equation, such methods are still limited to small systems containing ∼100-200 atoms and short time scales in molecular

dynamics. Therefore, treatment of larger systems mostly relies on the use of atomistic potentials that can be fitted to, e.g., DFT calculations. Given that reliable interatomic potentials have been obtained, they can serve as input for larger scale calculations using the molecular dynamics or Monte-Carlo methods.

ReaxFF atomistic potentials have become increasingly useful for studies of different properties of large systems including organic chemical reactions, studies of the chemistry of interfaces and catalytic properties, because such potentials have been specially designed for the treatment of bond breaking and creation [14, 15]. In the past ten years the ReaxFF model has been successively applied to the studies of, e.g., Fe/Al/Ni alloys [16], oxidation of Pd surfaces and clusters [17], catalytic conversion of C/H/O molecules on Cu-metal and Cu-oxide surfaces [18], ethanol oxidation [19], and Pt–Ni alloy catalyst [20].

In view of the importance of Au–Pd alloy for catalytic applications, in this work we develop a ReaxFF potential valuable for both bulk phase and small nanoparticles. Earlier, separate Au and Pd ReaxFF potentials were developed for the Au–S–C–H [21] and Pd/O [17] systems, respectively, however no combined Au–Pd potential is currently available. The force field parameterization was performed against density functional theory calculations of different bulk phases of the binary alloy, Au–Au, Au–Pd, and Pd–Pd dimer energies, as well as different slabs and nanoparticles (NP). We found several successful parametrizations and verify their validity on the calculations of bulk moduli, thermal expansion coefficients, melting temperature, and atomic order-disorder phenomena.

2. Methods

2.1. QM calculations

The reference data for potential development was obtained from density functional theory (DFT) calculations using the Vienna *ab initio* simulation package (VASP) [22, 23, 24]. Atomic core regions were represented with the projector augmented waves method [25]. The exchange correlation potential functional was treated by the generalized gradient approximation (GGA) in Perdew-Burke-Ernzerhof form [26]. The valence electron configurations for Pd and Au atoms are s^1d^{10} and s^1d^9, respectively. The plane wave basis cut off was 500 eV for all calculations. Calculations were performed with the 0.2 eV Methfessel-Paxton [27] smearing of order 1. The Brillouin zone was sampled with the 2×2×2 Monkhorst-Pack [28] mesh for bulk systems with 3×3×3 fcc cells. Calculation of (001) slabs was performed with 4×4×1 Γ-point mesh for 3×3×3 fcc cells with ≈38 Å vacuum spacing between the images in z direction corresponding to supercell size of approximately 12.5×12.5×50 Å. Nanoparticles with diameters ≈ 17 Å (∼200 atoms) were simulated in 42 Å cubic cells with the gamma point only.

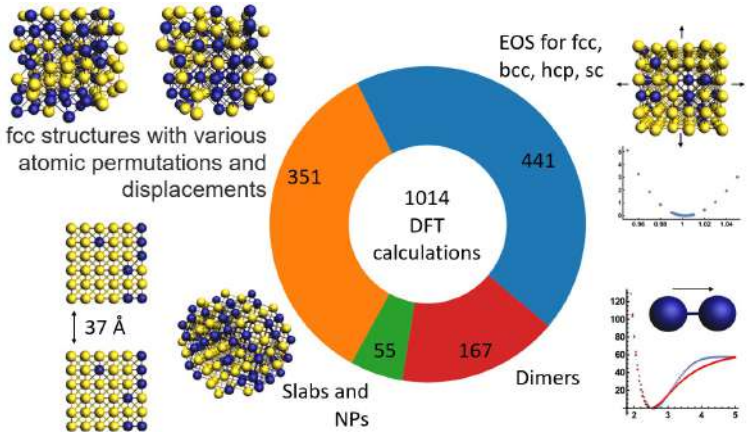

Figure 1. Schematic illustration of the training set for the ReaxFF Au–Pd potential development.

2.2. Force field optimization

Force field parameters were optimized with covariance matrix adaptation evolution strategy (CMA-ES) [29] algorithm as implemented in the AMS modeling package [30, 14, 31]. The optimization is stopped when the step-size becomes smaller than 10^{-6} for every parameter or optimization exceeds 10000 steps. In total 72 parameters were simultaneously fitted to training data with 100 samples in population. Since CMA-ES algorithm is stochastic, 80 runs were performed to find best force field parameters. Training data consisted of 1014 DFT calculations as shown in Fig. 1 and contain equations of state (EOS) for face-centered cubic (fcc), body-centered cubic (bcc), hexagonal closed-packed (hcp), and simple cubic (sc) structures, fcc and bcc structures with different atomic displacements and permutations of Au and Pd atoms among the lattice sites, Au–Au, Au–Pd, and Pd–Pd dimer energies, slabs, and nanoparticles. The structures included Au–Pd alloys with 0, 25, 50, 75, and 100 at.% Pd, which we in the following denote as AuPd0, AuPd25, AuPd50, AuPd75, and AuPd100, respectively.

2.3. Molecular dynamics and Monte-Carlo calculations

Molecular dynamics (MD) and Monte-Carlo (MC) simulations with developed ReaxFF potential were performed in LAMMPS package [32, 33]. MD simulations were carried out in 10×10×10 fcc cells systems with Nose-Hoover thermostat and barostat with 3 fs damping constant. The timestep was set to 0.1 fs.

Monte-Carlo atom swaps were employed to investigate ordering of Au–Pd systems. The simulation box contained 2048 atoms for bulk systems (8×8×8 fcc cells) and 2214 atoms for spherical nanoparticles. During the study of the order-disorder processes the temperature was lowered from 800 K (for bulk) or 1200 K (for nanoparticles) down to 20 K in steps of 10 K. After each step MC calculations were performed with 150 swap attempts per atom.

3. Results and discussion

3.1. ReaxFF force field development

In the development of the ReaxFF interatomic potential we follow the approach of Shin et al. [34] who have included three-body interactions in the treatment of Ni-Cr alloys, which helped achieving higher accuracy in description of their mechanical and thermal properties. The importance of three-body interactions is also supported by the failure of the Cauchy relation for elastic constants of Au and Pd, which should hold for centrosymmetric structures with only pair atomic interactions [35, 36], as well as by DFT-based cluster expansion calculations [37]. In fact, we have tried training and developing the ReaxFF potentials for the Au–Pd system without these three-body interactions, but obtained poor results. Therefore, the system energy was written as

$$E = E_{\text{bond}} + E_{\text{over}} + E_{\text{angle}} + E_{\text{vdW}} + E_{\text{Coul}}, \tag{1}$$

where E_{bond} is the bond energy, E_{over} is the over-coordination penalty energy, E_{angle} is the three-body valence angle strain, and E_{vdW} and E_{Coul} are van der Waals and Coulomb interactions, respectively [15]. The ReaxFF force field parameters were optimized against the DFT data as described in Sec. 2. In total 80 different ReaxFF potentials were obtained during the training, many of which showed good performance with respect to the training set. Final selection of the potentials was done by assessing their performance against a validation set of DFT data. The validation set included 225 and 100 fcc and bcc structures, respectively, as well as 42 nanoparticles, which had different permutations of Au and Pd atoms among the lattice sites and different displacements from ideal positions. Thus, we have selected four ReaxFF potentials that have similar performance against both the training and validation sets of DFT data. In the following we denote these ReaxFF potentials as RF1, RF2, RF3, and RF4. The obtained potentials are compared in Tables 1 and 2 and Figs. 3-5.

Figure 2 shows the variation of the energy per atom as function of the uniform compression a/a_0 of the lattice parameter a around the equilibrium value a_0. RF1 ReaxFF potential shows excellent agreement with DFT calculations for fcc and bcc structures with different concentrations of Pd. The performances of other ReaxFF potentials RF2, RF3, and RF4 are similar to that of RF1. Table 1 reports relative energy differences between different bulk phases for various Pd concentrations. As expected, the most stable structure is fcc and the energy differences are sufficiently well described by the four obtained ReaxFF potentials.

Figure 3 shows the performance plots of RF1-4 potentials for fcc structures in the training set with (i) different random atomic displacements and (ii) various Au and Pd permutations over the lattice sites, whereas ReaxFF predictions for slabs and nanoparticles is shown in Fig. 4. The R^2 coefficient of determination for the fcc structures exceeds 0.99, while the performance for slabs and NP's by ReaxFF potentials is lower, which is due to smaller percentage of these structures in the training set.

The second step in construction of the model potential is the validation. The

Table 1. Comparison of relative stability between different bulk phases of Au–Pd alloys: face-centered cubic (fcc), body-centered cubic (bcc), simple cubic (sc), and hexagonal closed-packed (hcp).

Energy difference, kcal/(mol·at.)		DFT	RF1	RF2	RF3	RF4
$\Delta E_{\mathrm{bcc-fcc}}$	AuPd0	0.3888	0.4834	0.5014	0.4225	0.4381
	AuPd50	1.1281	0.7733	0.7226	0.3883	0.9224
	AuPd100	0.8257	0.8975	0.7716	0.9325	0.9814
$\Delta E_{\mathrm{sc-fcc}}$	AuPd0	9.9999	15.863	10.998	17.389	15.606
	AuPd50	10.038	17.780	16.186	18.471	18.700
	AuPd100	11.044	17.250	19.630	16.701	15.091
$\Delta E_{\mathrm{hcp-fcc}}$	AuPd0	0.3835	0.3679	0.3782	0.3718	0.3722
	AuPd100	0.8183	0.7121	0.3351	0.3451	0.4618

structures and their energies in the validation set were not included in the training procedure. The assessment of the performance of ReaxFF potentials against the validation set is shown in Fig. 5. The R^2 coefficients of determination are above 0.99 for the bulk structures, which is similar to the performance with respect to the training set. The obtained ReaxFF potentials perform quite well even for large distortions of the lattice when the energy difference per atom relative to the undistorted structure reaches 4.5 kcal/(mol·at.). The mean error of ReaxFF prediction of the DFT data for both the training and validation sets is of the order of 0.1 kcal/(mol·at.), which correspond to the uncertainties ca. 50 K in the simulations of temperature dependent properties.

The four selected ReaxFF potentials describe the Au–Pd bulk alloys and small particles with a similar quality. However, their parametrizations are quite different as is clear from Table 2. One can note that the sigma bond covalent radius r_0^σ for Au is slightly higher than that of Pd in agreement with the relation between the atomic radii of these elements. These radii vary however from one potential to another by up to ≈0.15 Å. The Au-Pd (off-diagonal) sigma bond covalent radii fall inside the range of r_0^σ for Pd and Au for all potentials except RF2, where the radius of Au-Pd interaction r_0^σ is lower than that of Pd-Pd interaction (1.8685 vs 1.9163 Åcorrespondingly). The sigma bond dissociation energy D_e^σ for the Pd-Pd interaction also shows large variations between the potentials. Despite their different parametrization we show in the next section that all four ReaxFF potentials provide similar quality in macroscopic properties calculations.

3.2. Molecular dynamics and Monte-Carlo studies

Figures 6(a-e) show thermal expansion studies of 10×10×10 fcc structures. The thermal expansion coefficient at room temperature was determined by the linear fitting of the temperature dependence of the lattice constant. The fit results in the temperature range 200 – 400 K are given in Table 3. The linear expansion coefficients calculated in molecular dynamics are 10 to 40% lower than the experimental values with lower error

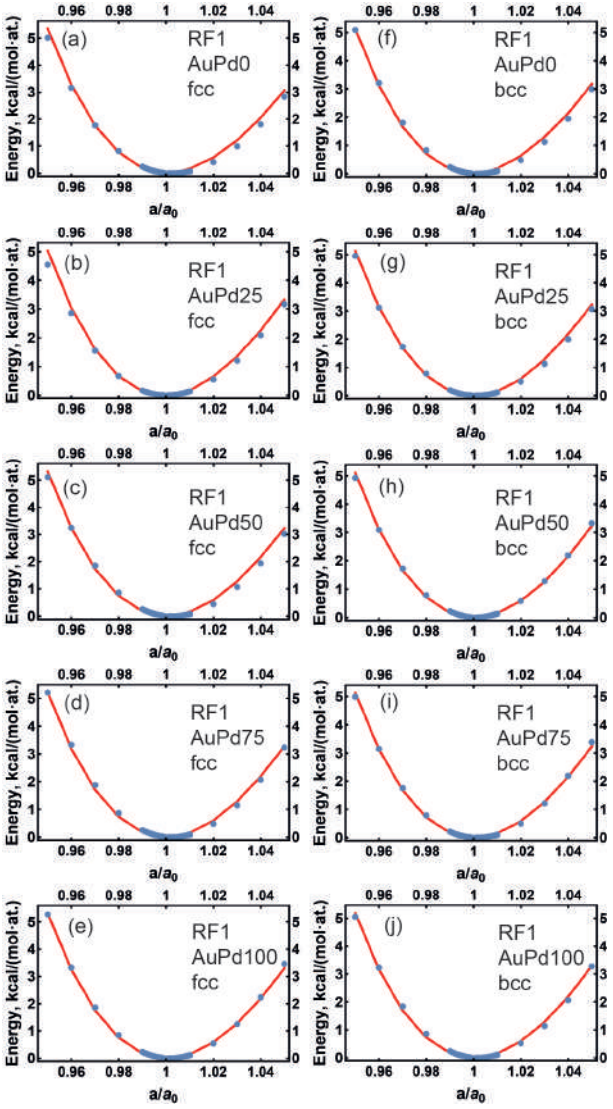

Figure 2. Comparison of the ReaxFF calculations (blue dots) using the RF1 potential with the DFT data (red lines) for the (a) – (e) fcc and (f) – (j) bcc structures.

for Au-rich alloys. The equation of state was probed by compression and expansion of 10×10×10 fcc structures at 300 K. Figs. 6(f-j) show the dependence of pressure P on the unit cell volume V. The bulk moduli B of bulk alloys with different Pd concentrations were determined by fitting the resulting $P(V)$ curves using the Birch-Murnaghan equation and are given in Table 3. The calculations reproduce the trend on decreasing lattice constant along with increasing Pd content. The larger value of the bulk modulus for pure Pd is obtained both in theory and experiment. However, ReaxFF calculations show systematic differences. For example the lattice parameters are overestimated by 2 %. This fact is explained by limitations of parent GGA-PBE DFT approximation as was demonstrated in [38].

Another type of validation criteria is related to the lattice dynamics. To determine the melting temperature the heating and cooling simulations of 8×8×8 unit cells

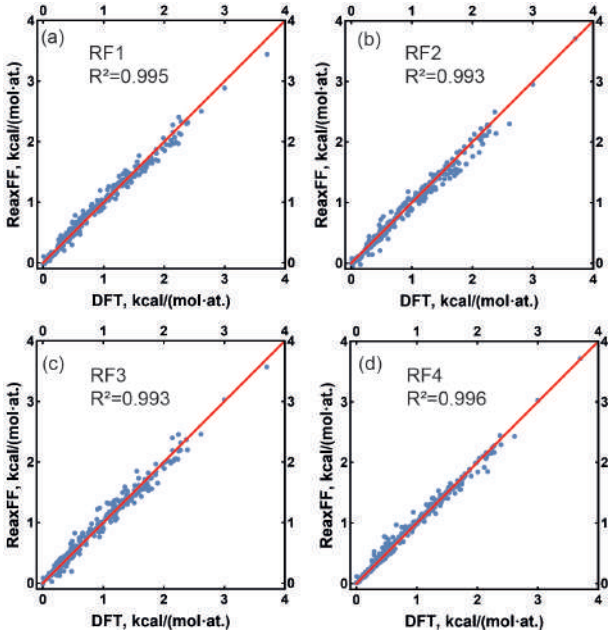

Figure 3. Performance of the ReaxFF calculations for different fcc structures for (a) – RF1, (b) – RF2, (c) – RF3, and (d) – RF4. Red line is guide to the eye.

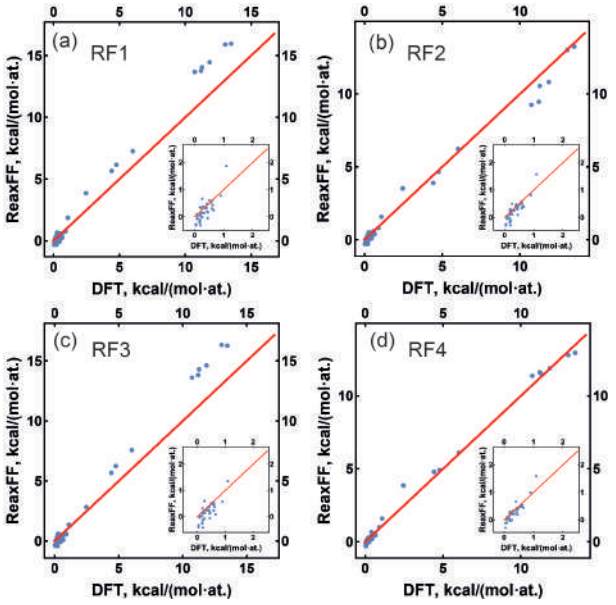

Figure 4. Performance of the ReaxFF calculations for different slabs and NP's for (a) – RF1, (b) – RF2, (c) – RF3, and (d) – RF4. The insets show enlarged areas of the parent graphs. Red line is guide to the eye.

fcc structures are performed. The resulting representative temperature dependencies of the density ρ are shown in Fig. 7. These data allow estimating the melting temperature using the approach of Luo et al. [39] by determining the temperatures T_+ and T_- of anomalies (jumps) in the densities during heating and cooling, respectively. The melting temperature T_m can then be calculated by $T_m = T_+ + T_- - \sqrt{T_+ T_-}$.

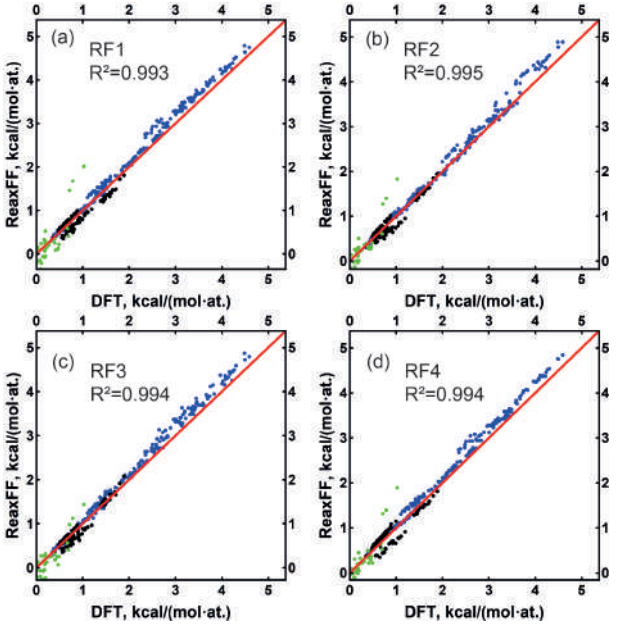

Figure 5. Validation set performance of the ReaxFF calculations for different fcc (blue dots) and bcc (black dots) structures, as well as for slabs and NP's (green dots) for (a) – RF1, (b) – RF2, (c) – RF3, and (d) – RF4. Red line is guide to the eye.

Table 2. Selected parameters of ReaxFF potentials. r_0^σ – sigma-bond covalent radius, r_vdW – van der Waals radius, γ – EEM shielding, χ – EEM electronegativity, η – EEM hardness, D_e^σ – sigma-bond dissociation energy.

ReaxFF potential	Au				
	r_0^σ	r_{vdW}	γ	χ	η
RF1	2.1338	1.9474	1.1211	3.0465	6.9417
RF2	2.0344	1.9825	0.9667	1.0681	8.9770
RF3	1.9907	1.8688	0.4869	5.2454	9.5167
RF4	2.1175	1.9391	0.4571	2.5850	9.3557
ReaxFF potential	Pd				
	r_0^σ	r_{vdW}	γ	χ	η
RF1	1.8631	2.6145	1.1143	5.4385	7.7107
RF2	1.9163	2.4185	1.1583	3.1622	7.4564
RF3	1.8359	2.3963	0.6400	5.4262	6.5508
RF4	1.8299	2.4460	0.7770	4.0514	8.5398

ReaxFF potential	Au-Au D_e^σ	Pd-Pd D_e^σ	Au-Pd D_e^σ	Au-Pd r_0^σ
RF1	128.7211	79.3679	102.5095	1.8968
RF2	137.7658	74.2573	102.4355	1.8685
RF3	129.3974	92.8535	112.2529	1.9391
RF4	136.6124	132.1784	110.6473	1.8936

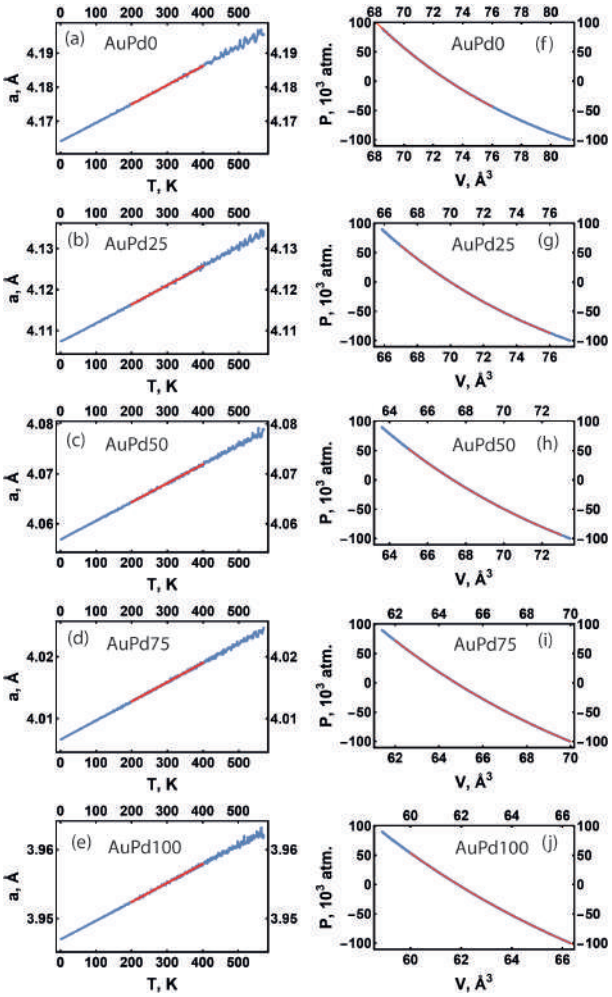

Figure 6. (a) - (e) Temperature dependencies of the lattice constant. Red lines represent linear fit. (f) - (j) The dependencies of pressure P on unit cell volume V. Red lines represent fits according to the Birch-Murnaghan equation.

Calculated melting temperatures are collected in Table 3 for all parameterized potentials. The molecular dynamics overestimates the melting temperatures, whereas the smaller thermal expansion coefficient for larger Pd concentration corresponds to the experiment and correlates with increasing melting temperature. Such deviations from the experimental values reflect the tendency of the GGA approximation to overestimate the lattice parameters and underestimate the bulk modulus [40].

One of the most important phenomena is the atomic ordering in alloys that can appear below a certain phase transition temperature. The ordering is a nonlocal process and, thus, represents another challenge for validation of the ReaxFF potentials. In the Au–Pd alloys in bulk form no long-range atomic ordering is observed experimentally arguably due to rather low phase transition temperatures. In bulk AuPd50, for example, the atomic ordering phase transition temperature was estimated to be about 100 °C from the temperature evolution of x-ray diffuse scattering, which reflected local short-range ordering [44]. In contrast, in thin films of AuPd25 and AuPd75 atomic ordering phase

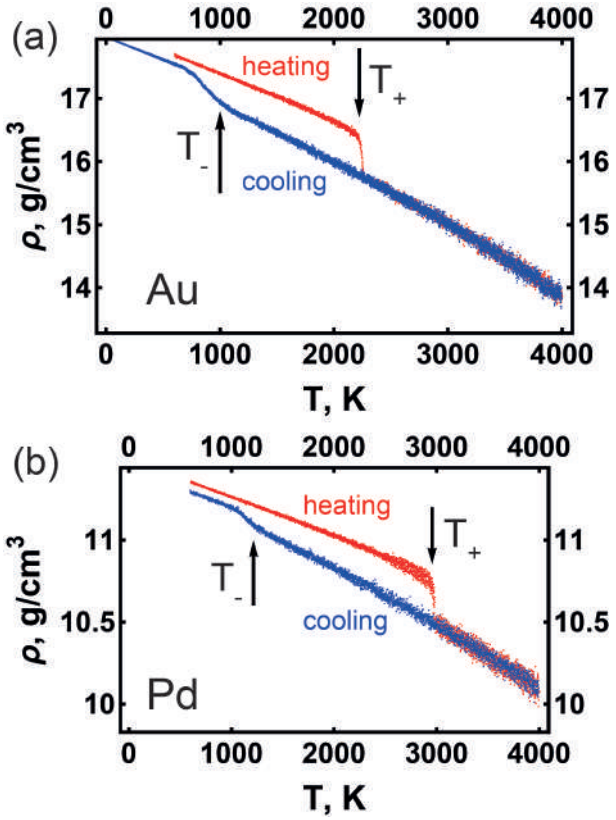

Figure 7. Calculated temperature dependence of the density upon heating and cooling using RF1 potential for the bulk Au (left) and Pd (right).

transition to the $L1_2$ structure (Cu_3Au type) is observed at ∼850 °C [45, 46]. Such a high phase transition temperature in films is likely a consequence of the in-plane strain.

Theoretically, the atomic ordering phase transition in Au–Pd has been studied in several works using DFT, DFT-based cluster expansion, and Monte-Carlo methods [47, 37, 48, 49, 50, 51]. The analysis of these data reveals that the chosen level of approximation influences the features of the temperature – concentration phase diagrams and the resulting ground state phases for different Au–Pd compositions. One can conclude that (i) the order-disorder phenomena can occur in the temperature range ∼250 – 400 K, (ii) the ground state for AuPd50 is the chalcopyritelike (CH) structure ($E1_1$ $CuFeS_2$ chalcopyrite type without sulfur atoms or equivalently the UPb type [52]), (iii) the ground state of AuPd75 is the $L1_2$ structure, and (iv) the ground state of AuPd25 is either of the $D0_{22}$, $D0_{23}$, or $L1_2$ structures with subtle energy differences between these structures making it difficult to determine the true ground state.

In our calculations the systems with 8×8×8 fcc unit cells of AuPd25, AuPd50, and AuPd75 were gradually cooled down from 800 to 20 K in steps of 10 K using constant pressure MD simulations. After each cooling step a Monte-Carlo atom-swap stage was performed. In each MC step 150 swap attempts per atom were made. The temperature dependencies of the relative ratios of successive swaps to the number of attempted swaps are shown in Figs. 8(a)-(c). Rapid decrease of the ratio of successive

Table 3. Molecular dynamics calculated lattice parameters a at 300 K, thermal expansion coefficients α, bulk moduli B, and melting temperatures T_m for different ReaxFF potentials. Experimental values are provided for comparison [41, 42, 43, 36].

ReaxFF potential	at. % Pd	a, Å	α, $10^{-6}\cdot K^{-1}$	B, GPa	T_m, K
RF1	0	4.18	13.4	122	1731
	25	4.12	11.4	130	
	50	4.07	9.3	141	
	75	4.02	7.8	153	
	100	3.95	7.0	167	2275
RF2	0	4.18	13.6	120	1391
	25	4.12	12.1	125	
	50	4.07	10.2	133	
	75	4.02	8.6	143	
	100	3.96	7.9	153	2367
RF3	0	4.18	13.7	122	1694
	25	4.12	11.4	127	
	50	4.07	9.1	140	
	75	4.02	7.8	153	
	100	3.96	7.9	166	2330
RF4	0	4.18	12.9	122	1582
	25	4.13	11.5	131	
	50	4.07	10.8	140	
	75	4.02	10.0	149	
	100	3.96	9.0	158	1940
exp.	0	4.0782	14.4	167	1337
	25	4.0272	12.5		
	50	3.98	12.0		
	75	3.9389	11.6		
	100	3.8896	11.9	190	1828

swaps upon cooling corresponds to quenching of atom swaps upon reaching local energy equilibrium. The quenching appears in the temperature range 250 – 400 K, which corresponds to the temperature range of order-disorder phase transitions found by previous theoretical calculations. The analysis of the temperature dependence of the lattice constants or unit cell volume shown in Figs. 8(d)-(f) confirms the presence of order-disorder phase transitions in bulk AuPd25, AuPd50, and AuPd75. In AuPd25 the phase transition occurs from cubic (sp. gr. $Fm\bar{3}m$) to the tetragonal $D0_{22}$ structure (sp. gr. I4/mmm), and is accompanied by the splitting of the $a = b$ and c lattice parameters as shown in Fig. 8(d) below T_c(AuPd25)=320 K. Here the lattice parameters are calculated by dividing the simulation box sizes in each direction by the number of unit cells in the simulation box along these directions. In AuPd50 the phase transition is to the tetragonal CH structure with sp. gr. $I4_1/amd$ reflected by splitting of the temperature dependence of the lattice parameters below T_c(AuPd50)=300 K shown in

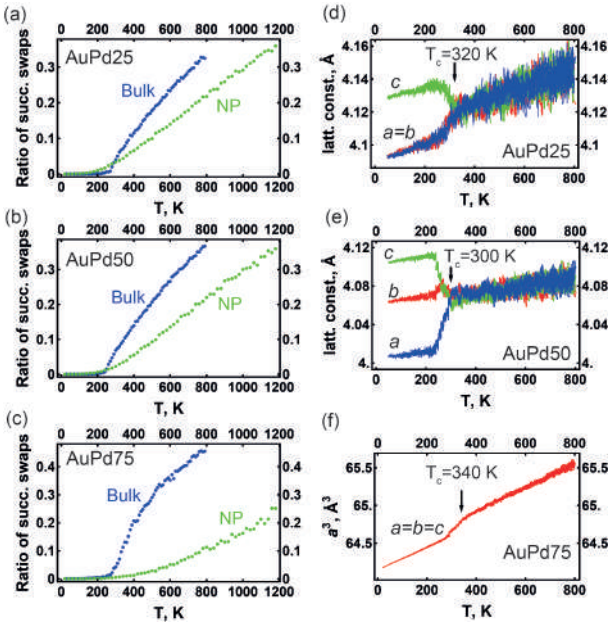

Figure 8. (a)–(c) Temperature dependence of the ratio of successive atom swaps in MC calculations normalized to the number of swap attempts. Blue and green dots are for bulk and nanoparticles, respectively. (d) and (e) Temperature dependence of the lattice constants of AuPd25 and AuPd50, respectively, during MD+MC cooling. Different colors correspond to lattice constants along different directions. (f) Temperature dependence of the unit cell volume of AuPd75 during MD+MC cooling.

Fig. 8(e). In our MD+MC simulations the AuPd50 system easily splits into domains, which results in complete splitting of a, b, and c in Fig. 8(e), however a smaller system with size 6×6×6 shows a phase transition to a single domain state with CH structure. The AuPd75 alloy upon ordering experiences a phase transition to the $L1_2$ structure with cubic symmetry $Pm\bar{3}m$ below T_c(AuPd75)=340 K, which is better observed in the temperature dependence of the unit cell volume $V = a^3$ shown in Fig. 8(f). Thus, the low temperature structures of AuPd25, AuPd50, and AuPd75 after MD+MC calculations are the $D0_{22}$, CH, and $L1_2$ structures as shown in Fig. 9. This result is in agreement with the earlier theoretical predictions using cluster expansion methods [48].

The ordering and distribution of atoms in spherical nanoparticles with diameter ∼4 nm (2214 atoms) were studied using similar combined MD+MC calculations. The temperature dependence of the ratio of successive swaps is shown in Figs. 8(a-c) for AuPd25, AuPd50, and AuPd75 NPs by green dots. This ratio gradually decreases with decreasing temperature indicating either some ordering or the freezing of atomic swapping processes. Similar to the bulk studies, complete quenching of swaps occurs at ∼250 K. Figures 10(a)-(c) show the structure of spherical nanoparticles at different Pd concentrations and temperatures. In AuPd25 the Pd atoms are uniformly distributed over the volume of the nanoparticle in the whole temperature range. On the contrary, AuPd50 NPs the atomic distribution of Au and Pd over the volume is uniform at 1200 K, whereas Au atoms tend to the surface of the NP upon decreasing the temperature, as

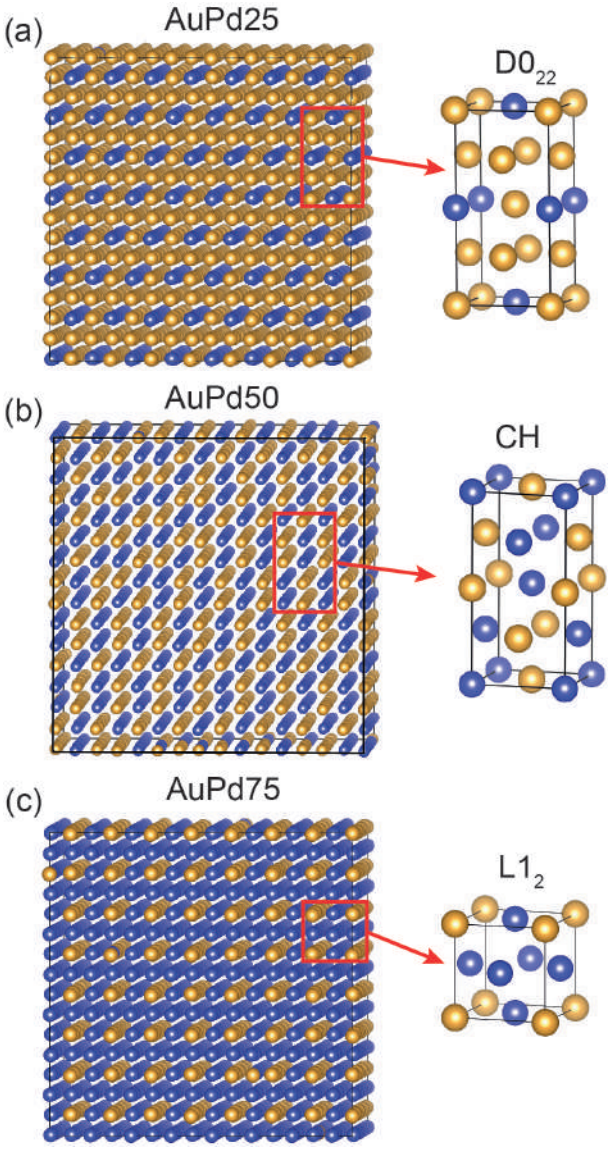

Figure 9. Low temperature structures of AuPd25 (a), AuPd50 (b), and AuPd75 (c). Gold and blue spheres represent Au and Pd atoms, respectively.

follows from the cross-section at 20 K. In AuPd75 already at 1200 K the Au atoms prefer the sites closer to the surface.

4. Conclusions

We present accurate ReaxFF potentials for the Au–Pd system valid for both bulk phase and nanoparticles. The task of potential parametrization has nonunique solutions. Assessment of potential performance against the validation set of DFT data allowed isolating four different potentials out of eighty that perform equally well both on the training and validation sets. Selected potentials have different parameters for the sigma bond covalent radii for Au and Pd as well as for sigma bond dissociation

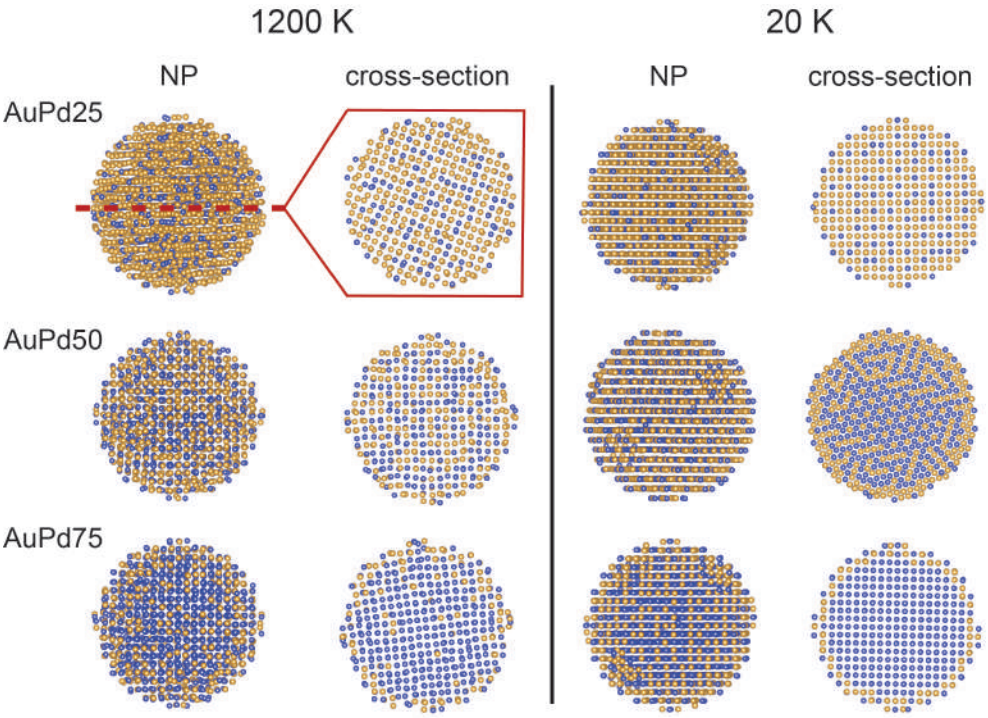

Figure 10. Structures of spherical nanoparticles and of their equatorial cross-sections at 1200 and 20 K after MD+MC cooling calculation for AuPd25 (upper row), AuPd50 (middle row), and AuPd75 (bottom row). Gold and blue spheres represent Au and Pd atoms, respectively.

energies. Despite the differences all potentials perform well in molecular dynamics and Monte-Carlo studies of various static and thermal physical properties. Selecting the unique solution requires additional validation criteria. We believe that the developed potentials will not be limited to the Au-–Pd system. Future extension to the interactions with organic molecules will make them capable of simulating heterogeneous catalytic reactions.

Acknowledgments

The authors acknowledge the Ministry of Science and Higher Education of the Russian Federation for financial support of ReaxFF potential development (Agreement № 075-15-2021-1363). The MD+MC part of the work was supported by the Strategic Academic Leadership Program of the Southern Federal University ("Priority 2030").

The authors acknowledge Prof. A.C.T. van Duin for his kind recommendations and the introduction in the details of ReaxFF calculations. Yu. Rusalev acknowledges Mike Pols for practical tips on selecting the parameters for optimization.

References

[1] K Sheng, D Luan, H Jiang, F Zeng, B Wei, F Pang, and J Ge. Ni_xCo_y Nanocatalyst Supported by ZrO_2 Hollow Sphere for Dry Reforming of Methane: Synergetic Catalysis by Ni and Co in Alloy. *ACS Applied Materials & Interfaces*, 11(27):24078–24087, 2019.

[2] T Kojima, S Kameoka, Sh Fujii, Sh Ueda, and A-P Tsai. Catalysis-tunable heusler alloys in selective hydrogenation of alkynes: A new potential for old materials. *Science Advances*, 4(10):eaat6063, 2018.

[3] Y Sun, B Huang, Y Li, Y Xing, M Luo, N Li, Zh Xia, Y Qin, D Su, L Wang, and Sh Guo. Trifunctional fishbone-like PtCo/Ir enables high-performance zinc-air batteries to drive the water-splitting catalysis. *Chem. Mater.*, 31(19):8136–8144, 2019.

[4] Q Shi, Ch Zhu, H Zhong, D Su, Na Li, M H Engelhard, H Xia, Q Zhang, Sh Feng, S P Beckman, D Du, and Y Lin. Nanovoid incorporated Ir_xCu metallic aerogels for oxygen evolution reaction catalysis. *ACS Energy Letters*, 3(9):2038–2044, 2018.

[5] Sh Tokonami, N Morita, K Takasaki, and N Toshima. Novel synthesis, structure, and oxidation catalysis of Ag/Au bimetallic nanoparticles. *J. Phys. Chem. C*, 114(23):10336–10341, 2010.

[6] Y-Ch Tsao, S Rej, Ch-Y Chiu, and M H Huang. Aqueous phase synthesis of au-ag core-shell nanocrystals with tunable shapes and their optical and catalytic properties. *J. Am. Chem. Soc.*, 136(1):396–404, 2014.

[7] Y Zhang, X Liu, T Liu, X Ma, Y Feng, B Xu, W Cai, Y Li, D Su, Q Shao, and X Huang. Rhombohedral pd–sb nanoplates with pd-terminated surface: An efficient bifunctional fuel-cell catalyst. *Adv. Mater.*, 34(31):2202333, 2022.

[8] J Fan, H Du, Y Zhao, Q Wang, Y Liu, D Li, and J Feng. Recent progress on rational design of bimetallic pd based catalysts and their advanced catalysis. *ACS Catalysis*, 10(22):13560–13583, 2020.

[9] M Chen, D Kumar, Ch-W Yi, and D W Goodman. The promotional effect of gold in catalysis by palladium-gold. *Science*, 310(5746):291–293, 2005.

[10] N Agarwal, S J Freakley, R U McVicker, S M Althahban, N Dimitratos, Q He, D J Morgan, R L Jenkins, D J Willock, S H Taylor, C J Kiely, and G J Hutchings. Aqueous au-pd colloids catalyze selective CH_4 oxidation to CH_3OH with O_2 under mild conditions. *Science*, 358(6360):223–227, 2017.

[11] Y Wang, L Cao, N J Libretto, X Li, Ch Li, Y Wan, C He, J Lee, J Gregg, H Zong, D Su, J T Miller, T Mueller, and Ch Wang. Ensemble effect in bimetallic electrocatalysts for CO_2 reduction. *J. Am. Chem. Soc.*, 141(42):16635–16642, 2019.

[12] L Wang, S Zhao, Ch Liu, Ch Li, X Li, H Li, Y Wang, Ch Ma, Zh Li, and J Zeng. Aerobic oxidation of cyclohexane on catalysts based on twinned and single-crystal $Au_{75}Pd_{25}$ bimetallic nanocrystals. *Nano Letters*, 15(5):2875–2880, 2015.

[13] B W J Chen, L Xu, and M Mavrikakis. Computational methods in heterogeneous catalysis. *Chemical Reviews*, 121(2):1007–1048, 2021.

[14] A C T van Duin, S Dasgupta, F Lorant, and W A Goddard. ReaxFF: A reactive force field for hydrocarbons. *J. Phys. Chem. A*, 105(41):9396–9409, 2001.

[15] K Chenoweth, A C T van Duin, and W A Goddard. ReaxFF reactive force field for molecular dynamics simulations of hydrocarbon oxidation. *J. Phys. Chem. A*, 112(5):1040–1053, 2008.

[16] Y K Shin, H Kwak, Ch Zou, A V Vasenkov, and A C T van Duin. Development and validation of a ReaxFF reactive force field for Fe/Al/Ni alloys: Molecular dynamics study of elastic constants, diffusion, and segregation. *J. Phys. Chem. A*, 116(49):12163–12174, 2012.

[17] T P Senftle, R J Meyer, M J Janik, and A C T van Duin. Development of a ReaxFF potential for Pd/O and application to palladium oxide formation. *J. Chem. Phys.*, 139(4):044109, 2013.

[18] W Zhu, H Gong, Y Han, M Zhang, and A C T van Duin. Development of a reactive force field for simulations on the catalytic conversion of C/H/O molecules on Cu-metal and Cu-oxide surfaces and application to Cu/CuO-based chemical looping. *J. Phys. Chem. C*, 124(23):12512–12520,

2020.

[19] S Arvelos and C E Hori. ReaxFF study of ethanol oxidation in O_2/N_2 and O_2/CO_2 environments at high temperatures. *J. Chem. Inform. Modeling*, 60(2):700–713, 2020.

[20] Y K Shin, L Gai, S Raman, and A C T van Duin. Development of a ReaxFF reactive force field for the Pt-Ni alloy catalyst. *J. Phys. Chem. A*, 120(41):8044–8055, 2016.

[21] T T Järvi, A C T van Duin, K Nordlund, and W A Goddard. Development of interatomic ReaxFF potentials for Au–S–C–H systems. *J. Phys. Chem. A*, 115(37):10315–10322, 2011.

[22] G Kresse and J Hafner. Ab initio molecular dynamics for liquid metals. *Phys. Rev. B*, 47:558–561, Jan 1993.

[23] G Kresse and J Furthmüller. Efficient iterative schemes for ab initio total-energy calculations using a plane-wave basis set. *Phys. Rev. B*, 54:11169–11186, Oct 1996.

[24] G Kresse and J Furthmüller. Efficiency of ab-initio total energy calculations for metals and semiconductors using a plane-wave basis set. *Computational Materials Science*, 6(1):15–50, 1996.

[25] G Kresse and D Joubert. From ultrasoft pseudopotentials to the projector augmented-wave method. *Phys. Rev. B*, 59:1758–1775, Jan 1999.

[26] John P Perdew, Kieron Burke, and Matthias Ernzerhof. Generalized gradient approximation made simple. *Phys. Rev. Lett.*, 77:3865–3868, Oct 1996.

[27] M Methfessel and A T Paxton. High-precision sampling for brillouin-zone integration in metals. *Phys. Rev. B*, 40:3616–3621, Aug 1989.

[28] H J Monkhorst and J D Pack. Special points for brillouin-zone integrations. *Phys. Rev. B*, 13:5188–5192, Jun 1976.

[29] Nikolaus Hansen. *The CMA Evolution Strategy: A Comparing Review*, pages 75–102. Springer Berlin Heidelberg, Berlin, Heidelberg, 2006.

[30] ReaxFF 2022.1, SCM, Theoretical Chemistry, Vrije Universiteit, Amsterdam, The Netherlands, http://www.scm.com.

[31] K Chenoweth, A C T van Duin, and W A Goddard. ReaxFF reactive force field for molecular dynamics simulations of hydrocarbon oxidation. *The Journal of Physical Chemistry A*, 112(5):1040–1053, 2008. PMID: 18197648.

[32] A P Thompson, H M Aktulga, R Berger, D S Bolintineanu, W M Brown, P S Crozier, P J in 't Veld, A Kohlmeyer, S G Moore, T D Nguyen, R Shan, M J Stevens, J Tranchida, C Trott, and S J Plimpton. LAMMPS - a flexible simulation tool for particle-based materials modeling at the atomic, meso, and continuum scales. *Comp. Phys. Comm.*, 271:108171, 2022.

[33] H M Aktulga, J C Fogarty, S A Pandit, and A Y Grama. Parallel reactive molecular dynamics: Numerical methods and algorithmic techniques. *Parallel Computing*, 38:245–259, 2012.

[34] Y K Shin, Y Gao, D Shin, and A C T van Duin. Impact of three-body interactions in a ReaxFF force field for Ni and Cr transition metals and their alloys on the prediction of thermal and mechanical properties. *Comp. Mater. Sci.*, 197:110602, 2021.

[35] Y A Chang and L Himmel. Temperature dependence of the elastic constants of Cu, Ag, and Au above room temperature. *J. Appl. Phys.*, 37(9):3567–3572, 1966.

[36] D K Hsu and R G Leisure. Elastic constants of palladium and β-phase palladium hydride between 4 and 300 k. *Phys. Rev. B*, 20:1339–1344, 1979.

[37] S V Barabash, V Blum, S Müller, and A Zunger. Prediction of unusual stable ordered structures of Au-Pd alloys via a first-principles cluster expansion. *Phys. Rev. B*, 74:035108, 2006.

[38] Ph Haas, F Tran, and P Blaha. Calculation of the lattice constant of solids with semilocal functionals. *Phys. Rev. B*, 79:085104, 2009.

[39] Sh-N Luo, A Strachan, and D C Swift. Nonequilibrium melting and crystallization of a model Lennard-Jones system. *J. Chem. Phys.*, 120(24):11640–11649, 2004.

[40] P Janthon, S A Luo, S M Kozlov, F Viñes, J Limtrakul, D G Truhlar, and F Illas. Bulk properties of transition metals: A challenge for the design of universal density functionals. *J. Chem. Theory Comput.*, 10(9):3832–3839, 2014.

[41] A Maeland and T B Flanagan. Lattice spacings of gold–palladium alloys. *Can. J. Phys.*, 42(11):2364–2366, 1964.

[42] H Okamoto and T B Massalski. The Au-Pd (gold-palladium) system. *Bull. Alloy Phase Diag.*, 6(3):229–235, 1985.

[43] D L Heinz and R Jeanloz. The equation of state of the gold calibration standard. *J. Appl. Phys.*, 55(4):885–893, 1984.

[44] V I Iveronova and A A Katsnel'son. Short-range order in a gold-palladium alloy of equiatomic composition. *Sov. Phys.–Crystallogr.*, 11:504, 1967.

[45] A Nagasawa, Y Matsuo, and J Kakinoki. Ordered alloys of gold-palladium system. I. electron diffraction study of evaporated Au_3Pd films. *J. Phys. Soc. Jpn.*, 20(10):1881–1885, 1965.

[46] Y Matsuo, A Nagasawa, and J Kakinoki. Ordered alloys of the gold-palladium system. II. electron diffraction study on evaporated $AuPd_3$ films. *J. Phys. Soc. Jpn.*, 21(12):2633–2637, 1966.

[47] S Curtarolo, D Morgan, and G Ceder. Accuracy of ab initio methods in predicting the crystal structures of metals: A review of 80 binary alloys. *Calphad*, 29(3):163–211, 2005.

[48] M H F Sluiter, C Colinet, and A Pasturel. Ab initio calculation of the phase stability in au-pd and ag-pt alloys. *Phys. Rev. B*, 73:174204, 2006.

[49] I Atanasov and M Hou. Equilibrium ordering properties of au–pd alloys and nanoalloys. *Surface Science*, 603(16):2639–2651, 2009.

[50] B Schönfeld, C R Sax, and A V Ruban. Atomic ordering in Au-(42 to 50) at.% Pd: A diffuse scattering and first-principles investigation. *Phys. Rev. B*, 85:014204, 2012.

[51] F Berthier, J Creuze, T Gabard, B Legrand, M-C Marinica, and C Mottet. Order-disorder or phase-separation transition: Analysis of the Au-Pd system by the effective site energy model. *Phys. Rev. B*, 99:014108, 2019.

[52] A Brown. The crystal structures of $ThPb_3$, UPb_3, ThPb and UPb. *Acta Cryst.*, 14(8):856–860, 1961.